IOP Publishing Nanotechnology
Nanotechnology 28 (2017) 064001 (17pp) doi:10.1088/1361-6528/aa5261

Quantum state readout of individual quantum dots by electrostatic force detection

Yoichi Miyahara, Antoine Roy-Gobeil and Peter Grutter

Department of Physics, McGill University, 3600 rue University, Montreal, H3A 2T8, Quebec, Canada

E-mail: yoichi.miyahara@mcgill.ca

Received 25 October 2016
Accepted for publication 8 December 2016
Published 6 January 2017

Abstract

Electric charge detection by atomic force microscopy (AFM) with single-electron resolution (e-EFM) is a promising way to investigate the electronic level structure of individual quantum dots (QDs). The oscillating AFM tip modulates the energy of the QDs, causing single electrons to tunnel between QDs and an electrode. The resulting oscillating electrostatic force changes the resonant frequency and damping of the AFM cantilever, enabling electrometry with a single-electron sensitivity. Quantitative electronic level spectroscopy is possible by sweeping the bias voltage. Charge stability diagram can be obtained by scanning the AFM tip around the QD. e-EFM technique enables to investigate individual colloidal nanoparticles and self-assembled QDs without nanoscale electrodes. e-EFM is a quantum electromechanical system where the back-action of a tunneling electron is detected by AFM; it can also be considered as a mechanical analog of admittance spectroscopy with a radio frequency resonator, which is emerging as a promising tool for quantum state readout for quantum computing. In combination with the topography imaging capability of the AFM, e-EFM is a powerful tool for investigating new nanoscale material systems which can be used as quantum bits.

Keywords: atomic force microscopy, quantum dot, electrostatic force microscopy, Coulomb blockade, single electron tunneling, quantum electromechanical system

(Some figures may appear in colour only in the online journal)

1. Introduction

Quantum dots (QDs) are one of the most interesting and important entities in nanoscience and nanotechnology. QDs are often called artificial atoms as their electronic states become discrete just like those in atoms because of quantum confinement in three dimensions. The emergence of atom-like discrete energy levels leads to particular optical and electronic properties of QDs. Unlike real atoms, one can engineer the size and shape of the QDs, leading to their tunable optical and electronic properties. Therefore, understanding the energy level structure and its relation to the shape and size of the QD is a key to understand the properties of QDs, which remains to be elucidated. For this end, spectroscopic measurement on individual QDs is essential. QDs have been attracting much attention in the field of quantum information processing as their atom-like discrete energy levels can host charge or spin qubit and their quantum state can be read out by probing the charge state of the QD [1]. Many studies have already been reported [2–4].

Current transport spectroscopy performed in single-electron transistor (SET) structures [5] has been instrumental to understanding the electronic levels of individual QDs. In a SET structure, the energy level of the QD can be shifted by the gate voltage with respect to the source and drain electrodes. When one of the energy levels of the QD lies in the bias window set by the source–drain bias, a single electron can tunnel through two tunnel barriers at the source-QD and the drain-QD. When the source–drain current is measured as a function of gate bias voltage, peaks appear in the conductance versus gate voltage curves. This is known as a Coulomb-blockade oscillation peak. The energy of these peaks is the

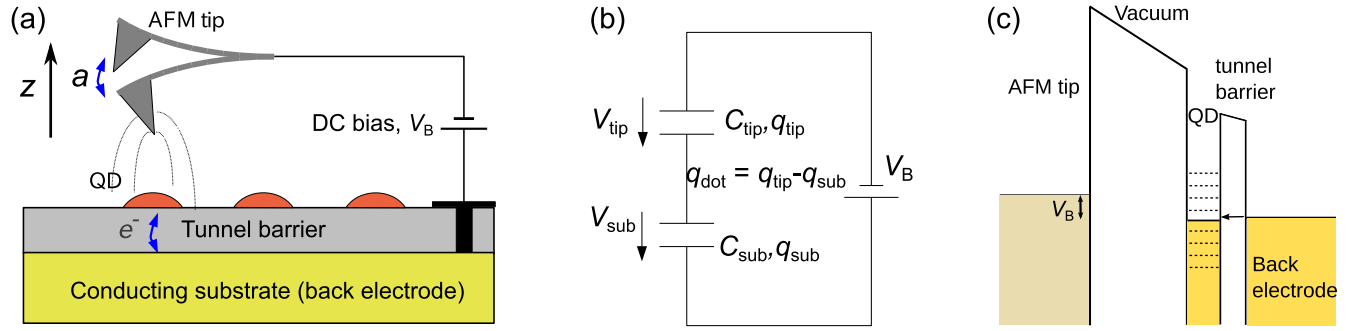

Figure 1. (a) Schematic of experimental setup. (b) Equivalent circuit of the system shown in (a). (c) Energy diagram of the system.

sum of the energy of the discrete levels and the Coulomb charging energy of the QD. A detailed analysis of these spacings thus allows the spectroscopy of the electronic energy levels of the QD [6]. Although current transport spectroscopy is very powerful, its application has been limited mainly to gate-defined QDs where a QD is formed in a two dimensional electron gas using surface gate electrodes to create a confinement potential.

Other interesting classes of QDs such as self-assembled QDs and colloidal nanoparticles (NPs) have not been studied as much by current transport spectroscopy because attaching electrodes to these QDs by lithography techniques is challenging due to their smaller sizes. Recently, NPs with more complex shape and structure have been developed for more functionalities such as biochemical sensing [7–9]. As attaching electrodes to these NPs and their complexes is even more challenging, current transport spectroscopy has not been done in most of these complex structures.

In order to overcome the difficulty, we have developed an alternative experimental technique (e-EFM). The charge state of the QD can be detected by electrostatic force microscopy with sensitivity much better than a single electron charge [10]. The AFM tip also acts as a scannable gate, thus enabling spectroscopic measurements of single electron charging. To enable these experiments, the QD needs to be tunnel-coupled to a back-electrode. Oscillating the AFM tip modulates the energy of the QD, causing a single electron back and forth to tunnel between the QD and back-electrode. The resulting oscillating electrostatic force changes the resonant frequency and damping of the AFM cantilever, enabling the sensitive electrometry with single-electron sensitivity.

As e-EFM requires no nanometer scale electrode to be attached to the QD, it makes it possible to investigate individual colloidal NPs and self-assembled QDs which pose major challenges for transport spectroscopy. This technique is equivalent to admittance spectroscopy with a radio frequency (RF) resonator, which is emerging as a promising tool for quantum state readout [11–13]. In combination with the topography imaging capability of the AFM, e-EFM can be a powerful tool for investigating new nanoscale material systems which can be used as quantum bits. The fundamental physics of e-EFM is also of great interest as the measured interaction between the AFM tip and QD can be described as a back-action of a measurements on quantum electromechanical system [14].

In this review, we will first describe the basic principle of operation of the technique, followed by its application to several experimental systems. We will then discuss more detailed theoretical aspects which lead to physical insights which we can gain by this technique. Finally, we will discuss prospect of the technique, including possible application to other physical systems.

2. Single-electron detection by force detection

2.1. Overview of technique

The experimental technique we describe here is essentially based on electrostatic force microscopy (EFM) which is a variant of atomic force microscopy (AFM). While AFM was shown to be capable of detecting a single-electron charge soon after its invention [10], this single-electron charge sensitivity has not been widely exploited.

Figure 1(a) depicts the experimental setup of our technique. QDs are separated from a conductive substrate (the back-electrode) by a tunnel barrier that allows electrons to tunnel between the QD and substrate. An oscillating conductive AFM tip is used as a sensitive charge detector as well as a movable (scannable) gate. A dc bias voltage is applied between the AFM tip and conductive substrate (back-electrode) to control the electron tunneling. The tip–QD distance is set to the order of 10 nm so that no tunneling is allowed across the vacuum gap between the tip and QD, making the system a so-called ‘single-electron box’ [15]. The system with only a single tunnel barrier has several important advantages both experimentally and theoretically as will be shown later.

Choice of an appropriate dc bias enables a single electron to tunnel back and forth in response to the oscillating energy detuning across the barrier which is induced by the tip oscillation. The tunneling single-electron thus produces an oscillating electrostatic force which causes peaks both in the resonance frequency and the damping (dissipation) of the AFM cantilever. As is shown later, these peaks are essentially equivalent to the Coulomb peaks usually observed in dc transport spectroscopy and capacitance/impedance spectroscopy on SETs [6, 16].

The frequency modulation (FM) mode operation [17] of AFM is used to detect the oscillating electrostatic force caused by the single-electron tunneling. Because of the finite

tunneling rate, there is a time delay for the oscillating force with respect to the tip motion. The in-phase component of the oscillating electrostatic force gives rise to the frequency shift signal and its quadrature component to the damping (dissipation) signal. The effect can also be described as a result of the quantum back-action of the tunneling electrons [14].

Another unique feature of this technique is the scanning capability which enables the spatial mapping of single-electron tunneling events. We will see that the spatial maps of the resonance frequency shift and dissipation are equivalent to the so-called charge stability diagram [18, 19] which provides a wealth of information particularly on the systems containing multiple QDs. The described technique, termed single-electron electrostatic force microscopy (e-EFM), was first demonstrated on QDs formed in carbon nanotube SETs [20–22]. As the present technique requires no patterned electrode to be defined around the QDs, it can open up the spectroscopy on individual QDs of various kinds that have been very difficult to investigate, such as colloidal NP dots and those having complex structures [7, 9, 23].

2.2. Electrostatic force in AFM tip–QD system

Following the equivalent circuit model commonly used in the QD transport studies [15], we model the system as shown in figure 1(b). The electrostatic force acting on an AFM tip shown in figure 1(a) can be calculated by considering electrostatic free energy of the system, W, which is shown below [24]:

$$W = \frac{q_{\mathrm{dot}}^2}{2C_\Sigma} + \frac{C_{\mathrm{tip}}}{C_\Sigma} q_{\mathrm{dot}} V_{\mathrm{B}} - \frac{1}{2}\frac{C_{\mathrm{sub}} C_{\mathrm{tip}}}{C_\Sigma} V_{\mathrm{B}}^2 \tag{1}$$

where q_{dot} is the electricalcharge in the QD, C_{tip} the tip–QD capacitance, C_{sub} the QD-back-electrode capacitance and $C_\Sigma \equiv C_{\mathrm{tip}} + C_{\mathrm{sub}}$.

Differentiating the electrostatic free energy with respect to the tip position, z, yields the expression for the electrostatic force as follows:

$$F_{\mathrm{elec}} = -\frac{\partial W}{\partial z} = \frac{1}{C_\Sigma^2}\frac{\partial C_{\mathrm{tip}}}{\partial z} \times \left\{ \frac{q_{\mathrm{dot}}^2}{2} - C_{\mathrm{sub}}\, q_{\mathrm{dot}}\, V_{\mathrm{B}} + \frac{1}{2} C_{\mathrm{sub}}^2 V_{\mathrm{B}}^2 \right\}. \tag{2}$$

The third term on the right-hand side represents the electrostatic interaction between the charges in the tip and conducting substrate (back-electrode) which is known as the capacitive force. This term is responsible for the parabolic background commonly observed in frequency shift versus bias voltage curves. The second term is proportional to the charge in the QD and responsible for the detection of single-electron tunneling. In the system shown in figure 1(a), the charge in the QD, $q_{\mathrm{dot}} = -ne$, (e: elementary charge) is determined by the number of electrons in the QD, n, and can be varied solely by the electron tunneling through the tunnel barrier to the substrate because of the much larger tunnel barrier height of the vacuum gap prohibiting the tunneling between tip–QD.

2.3. Coulomb blockade effect in a single QD system probed by electrostatic force detection

In order for a single electron to tunnel into the QD from the back-electrode, the final state must be more energetically favorable than the initial one. Considering the electron tunneling process between n electron state and $n + 1$ electron state, the free energy of two states needs to be equal to $W(n + 1) = W(n)$. This condition sets the threshold bias voltages for the tunneling to be

$$V_{\mathrm{B}}^{n+1} = \frac{e}{C_{\mathrm{tip}}}\left(n + \frac{1}{2}\right). \tag{3}$$

The separation of two successive peaks, $\Delta V_{\mathrm{B}} = e/C_{\mathrm{tip}}$, is proportional to so-called addition energy which represents the energy required to add an extra electron to the QD. In general, the addition energy, E_{add}, is determined not only by the Coulomb charging energy of the QD, $2E_{\mathrm{C}} = e^2/C_\Sigma$, but also the energy difference between consecutive quantum states, δ. E_{add} is related to ΔV_{B} through the relation $E_{\mathrm{add}} = e\alpha\Delta V_{\mathrm{B}}$ where α is the fraction of V_{B} applied across the tunnel barrier and given as $\alpha = C_{\mathrm{tip}}/C_\Sigma$. α is often called the lever-arm. In order to get the true energy scale in the QD, α needs to be determined. As we will see later, α can be determined experimentally from the peak shape of the frequency shift or dissipation peak.

As α is determined by C_{tip} and C_{sub}, the oscillating tip leads to the oscillation of the QD energy levels through the oscillation of α. In other words, the oscillating tip causes the modulation of the energy level detuning, ΔE, across the tunnel barrier. At each V_{B}^{n+1}, a single electron can tunnel back and forth between the QD and back-electrode in response to the oscillation in the QD energy. It is this oscillating single electron that induces the peaks in frequency shift and dissipation. At low temperature, T, ($k_{\mathrm{B}}T \ll E_{\mathrm{add}}$, k_{B}: Boltzmann constant), the number of electron is fixed due to the large addition energy of the QDs between two adjacent peaks (Coulomb blockade).

The shape of the peaks can be derived by considering the equation of motion of the AFM cantilever that is subject to the oscillating electrostatic force caused by the tunneling single electron, F_{dot} as described below:

$$m\ddot{z} + m\gamma_0\dot{z} + k(z - z_0) = F_{\mathrm{ext}}(z, t) = F_{\mathrm{dot}}(t) + F_{\mathrm{exc}}(t) \tag{4}$$

where m, γ_0 and k are the effective mass, intrinsic damping and spring constant of the AFM cantilever, respectively. F_{exc} is the external driving force that is controlled by the self-oscillation electronics [17].

The second term of equation (2), F_{dot}, is the back-action of the tunneling process on the detector (i.e. AFM cantilever) and is given by:

$$F_{\mathrm{dot}}(t) = -\frac{C_{\mathrm{sub}}}{C_\Sigma^2}(q_{\mathrm{dot}}\, V_{\mathrm{B}})\frac{\partial C_{\mathrm{tip}}}{\partial z} = -\frac{2E_{\mathrm{C}} V_{\mathrm{B}}}{e}(1 - \alpha)\frac{\partial C_{\mathrm{tip}}}{\partial z} n = An \tag{5}$$

where $A = -(2E_{\mathrm{C}} V_{\mathrm{B}}/e)(1 - \alpha)\partial C_{\mathrm{tip}}/\partial z$. A describes the

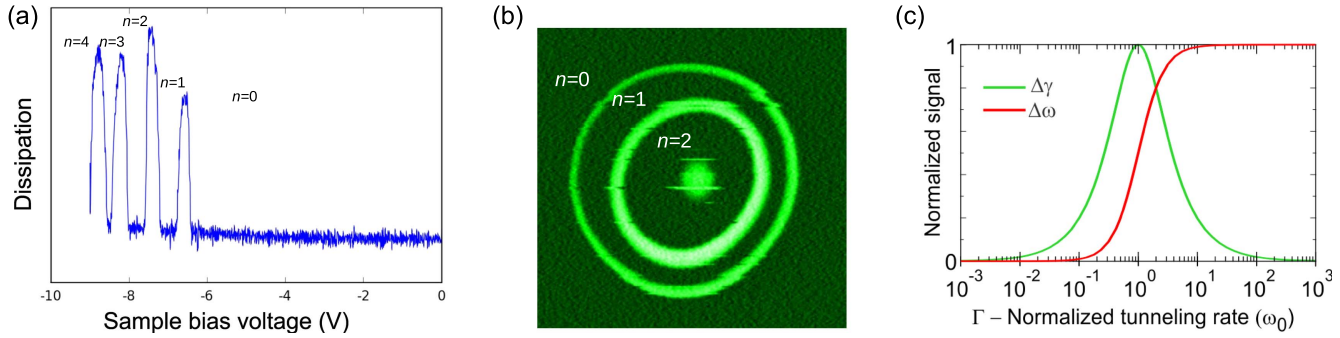

Figure 2. (a) Single-electron tunneling peaks in dissipation versus bias voltage curve. (b) Single-electron tunneling rings in the dissipation image taken at a constant bias voltage. Each peak in (a) corresponds to a ring in (b). (c) Normalized amplitude of Dissipation and frequency shift as a function of tunneling rate.

magnitude of the force due to the capacitive tip–QD coupling and is dependent on the geometry of the tip and QD and bias voltage. In practice, the tip–QD distance is a very important parameter and A increases with decreasing tip–QD distance.

Dynamics of the charge in the QD can be described by the master equation, $\partial\langle n\rangle/\partial t = -\Gamma_-(z)\langle n\rangle + \Gamma_+(z)(1-\langle n\rangle)$ where Γ_+ (Γ_-) are z-dependent tunneling rates to add (remove) an electron to the QD and $\langle n\rangle$ denotes the average number of electrons on the QD. The widely accepted treatment of single-electron tunneling implies that the operation of single-electron devices that is governed by stochastic tunneling events, can be described well by time-evolution of the average value [15].

For a small tip oscillation amplitude, considering a single non-degenerate level in the QD and the linear response of the average charge on the QD, the changes in frequency shift, $\Delta\omega$, and dissipation, $\Delta\gamma$, due to the single-electron tunneling are given as follows [25]:

$$\Delta\omega = -\frac{\omega_0^2 A^2}{2kk_{\mathrm{B}}T}\frac{1}{1+(\omega_0/\Gamma)^2}f(\Delta E)[1-f(\Delta E)] \quad (6)$$

$$\Delta\gamma = \frac{\omega_0^2 A^2}{kk_{\mathrm{B}}T}\frac{\omega_0/\Gamma}{1+(\omega_0/\Gamma)^2}f(\Delta E)[1-f(\Delta E)] \quad (7)$$

where ω_0 is the angular resonance frequency of the cantilever, Γ the tunneling rate between the QD and back-electrode and f the Fermi–Dirac distribution function. In this single non-degenerate level case, the tunneling rate is independent of the energy and equal to tunnel coupling constant. In general, however, the tunneling rate is energy-dependent and determined by the energy-level structure of the QD and back-electrode. We will see this aspect in the section 5.1. Note that each expression contains a prefactor containing the ratio between the oscillation frequency of the cantilever and the tunneling rate. The tunneling rate can thus be extracted directly by taking these ratio such as

$$\Gamma = -2\omega_0\frac{\Delta\omega}{\Delta\gamma} \quad (8)$$

In other words, the magnitude of $\Delta\omega$ and $\Delta\gamma$ depends on the ratio of the cantilever oscillation frequency to the tunneling rate, ω_0/Γ, as shown in figure 2(c). The magnitude of $\Delta\gamma$ takes its maximum when $\Gamma \approx \omega_0$. Note that this determines the condition for which both frequency shift and damping signals are observable [20, 22, 26, 27]. Specifically, the tunneling rate between the QD and the back-electrode needs to be engineered to be similar to the cantilever resonance frequency (to within a factor of 10). Note that the resonance frequency of AFM cantilevers is typically a few hundred kHz. As we will see later, this tunneling rate can be engineered by selecting a barrier of suitable thickness. In the later sections, we will see that the detailed analysis of the peak shape provide such useful information as shell-filling of the energy levels in the QD and the density-of-states of the QD levels.

2.4. Spatial mapping of charge state

Changing the distance between tip and QD changes the lever-arm and thus the energy between QD and back electrode. Since the AFM tip is a scannable gate and charge sensor, one can spatially map the charging events, a unique feature, not available in conventional transport measurements. The dissipation image shown in figure 2(b) demonstrates the unique capability of this technique. This image is taken by scanning the tip over a QD at a constant tip-height with a constant bias voltage while acquiring the frequency shift and dissipation signals. Each of the circular concentric rings in figure 2(b) correspond to a peak in the dissipation versus bias voltage spectrum (figure 2(a)) obtained at a fixed tip position (x, y, z).

The concentric rings can be understood by considering the energy diagram of the system. The energy detuning, ΔE, which governs the electron tunneling is dependent on the lever-arm, α, as well as V_{B}. In fact, α is a function of the tip position such as $\alpha(x, y, z)$ because the tip-sample capacitance depends on the tip position. If α depends only on the distance between a QD and tip such as $\alpha(x, y, z) = \alpha(r)$ where $r = \sqrt{(x-x_0)^2+(y-y_0)^2+(z-z_0)^2}$ $((x_0, y_0, z_0)$ denotes the position of the QD) [28], a specific ΔE allowing tunneling is mapped to a circular ring around the center of the QD. Although the real effect of the biased tip on the QD confinement potential can be more complex, this simple model has so far been able to explain most of the important features observed in experiments.

The image indicates that the number of electrons in the QD can be controlled by the tip position without changing V_{B}. It is true even for multiple QD complex as shown in

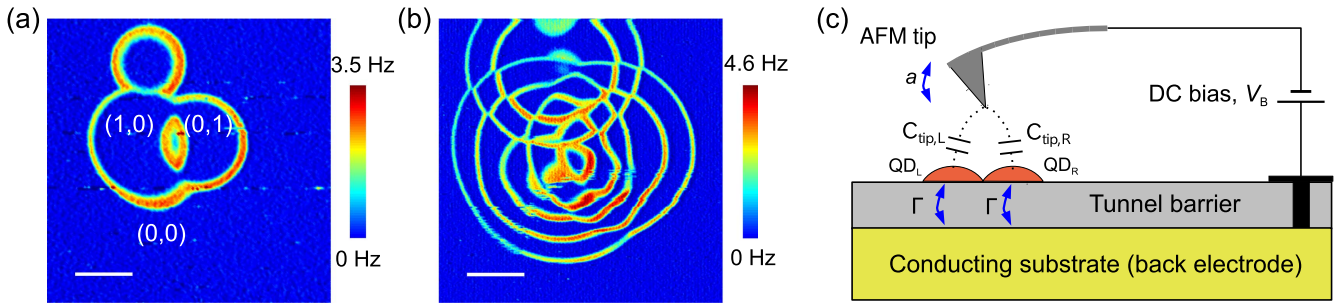

Figure 3. (a) and (b) Dissipation images of the same area containing three QDs taken at two different bias voltages, $V_B = -7.6$ V (a) and $V_B = -9.0$ V (b). The numbers in parenthesis in (a) indicate the number of electrons in the left and right QDs. Scalebar is 20 nm [25]. (c) Schematic showing different coupling capacitances to each QD.

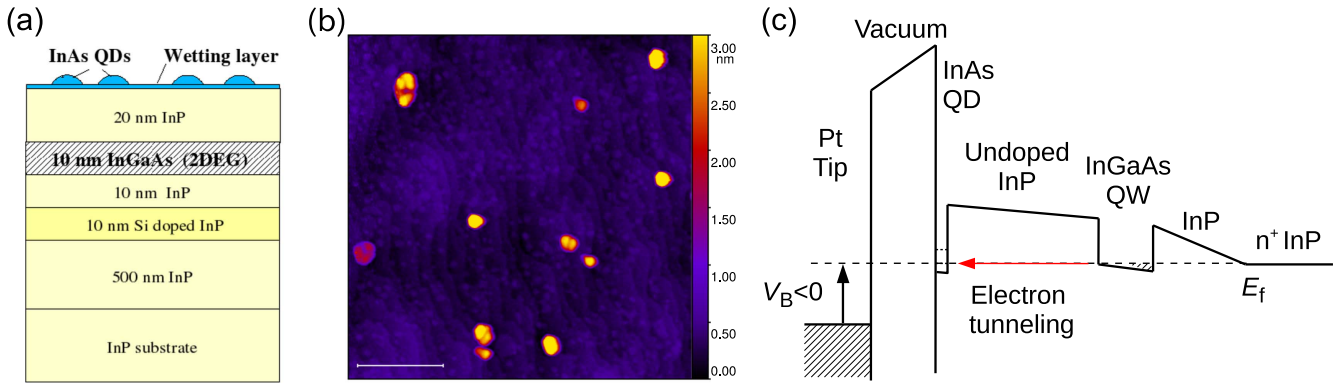

Figure 4. (a) Schematic of InAs QD on InP sample structure. (b) Tapping mode AFM topogaphy images of the InAs QD sample. Scale bar is 500 nm. (c) Energy diagram of the system.

figure 3(a) because even though there is only one gate (AFM tip), changing tip position change the lever-arm, α, for each QD, thus the energy of each QD (figure 3(c)). Figures 3(a) and (b) show the charging of three QDs located close to each other. We can see that the number of electrons in each QD can be controlled by the tip position. Furthermore, as expected, we observe avoided-crossings of the rings, indicative of the coupling between the QDs. In fact, these dissipation images are equivalent to the charge stability diagram [18] of multiple QDs as we will see more detail in the later section 4.3. Characterizing coupled-QDs is of great interest because if the inter-dot tunneling coupling is coherent, the QD complex should behave as an artificial molecule which can host a charge or spin qubit [3, 4].

3. Experimental

The experiments are performed with a home-built cryogenic atomic force microscope [29], in which a fiber optic interferometer is used for cantilever deflection sensing [30, 31]. A fiber-pigtailed laser diode operating at a wavelength of 1550 nm is used for the interferometer. The laser diode current is modulated by a RF signal through a bias-tee to reduce the coherence length of the laser to reduce phase noise and suppress undesirable interferences. A typical optical power of 100 μW is emitted from a cleaved optical fiber end. We use commercially available AFM cantilevers (NCLR, Nanosensors) with typical resonance frequency and spring constant of 160 kHz and 20 N m^{-1}, respectively. The tip side of the cantilevers are coated with 20 nm thick Pt/10 nm thick Ti by sputtering to ensure a good electrical conductivity even at liquid helium temperature. A dilute helium exchange gas ($\sim 10^{-3}$ mbar) is introduced in the vacuum can for the experiments at low temperature for good thermalization. The typical quality factor of the cantilevers ranges from 30 000 to 50 000 at 77 K and 100 000 to 200 000 at 4.5 K, which is unaffected by the exchange gas.

The fundamental flexural-mode oscillation is controlled either by a self-oscillation feedback electronics which consists of a phase shifter and an amplitude controller (Nanosurf EasyPLLplus) or by a digital phase-locked loop oscillation controller (Nanonis OC4). The resonance frequency shift is measured by a phase-locked loop frequency detector (Nanosurf EasyPLLplus or Nanonis OC4). The amplitude of the excitation signal is measured as a dissipation signal. Care must be taken to correct for the background dissipation signal caused by the non-flat frequency response of piezoacoustic excitation systems [32].

4. Epitaxially grown self-assembled InAs QD on InP

In our first experiment, we used epitaxially grown self-assembled InAs QDs [33]. The schematic of the structure and

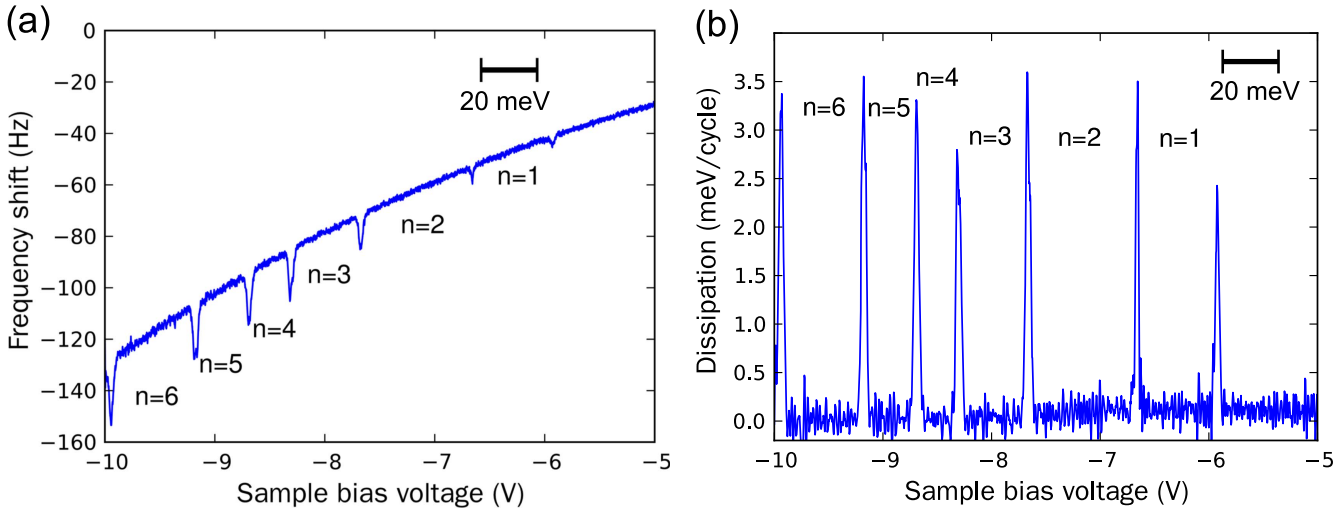

Figure 5. (a) Frequency shift and (b) Dissipation versus bias voltage spectra measured on an InAs QD shown in figure 4 at 4.5 K. The energy scale in the QD calculated from the lever-arm, $\alpha = 0.04$, is indicated as a scale bar in each figure.

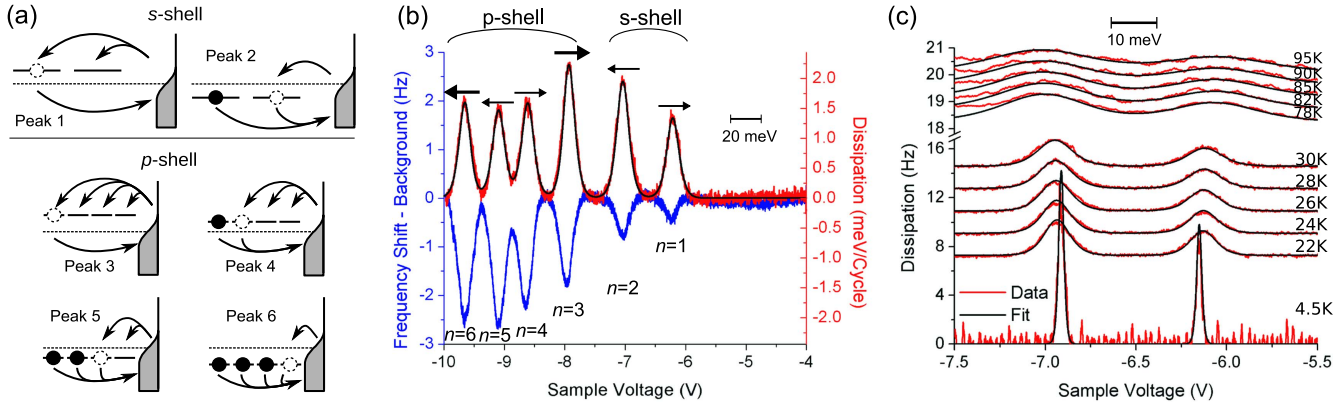

Figure 6. (a) Schematic representation of asymmetric tunneling processes. Solid horizontal lines depict electronic levels on the QD and the grayed area in the right-hand side depicts Fermi distribution of electrons in the back-electrode. The fine dashed line is where the chemical potentials line up and where a dissipation peak would occur for a nondegenerate level. (b) The measured dissipation and frequency shift versus bias curves measured at 30 K. The parabolic background is subtracted from the frequency shift spectrum. The energy scale in the QD is indicated as a scale bar (20 meV). The arrows indicate the directions of the peak shifts with increasing temperature. (c) The measured and fitted dissipation spectra as a function of temperature. The curves are fitted with equation (10). The energy scale in the QD is indicated as a scale bar (10 meV). Adapted from [25].

the energy level diagram of the sample are shown in figures 4(a) and (c). The two-dimensional electron gas (2DEG) layer formed in a InGaAs quantum well serves as a back-electrode which works at liquid helium temperature and the 20 nm thick undoped InP layer serves as a tunnel barrier. In this system, InAs islands are spontaneously formed after the growth of monolayer thick InAs wetting layer due to the lattice mismatch between InAs and InP. Figure 4(b) shows an AFM topography image of the sample surface. The variation in size and shape of the InAs QDs can be clearly seen, indicating the spectroscopy of individual QDs is highly desired.

Figure 5 shows typical bias-spectroscopy curves taken over one of the InAs QDs by sweeping the tip-sample bias voltage, V_B. While sharp dips appear in the frequency shift versus V_B curve on top of the parabolic background, sharp peaks appear in the dissipation versus V_B curve at the same bias voltages. When the sample is negatively biased, the electronic levels in the InAs QD are brought down with respect to the back-electrode (InGaAs quantum well) as shown in figure 4(c). At a sufficiently high negative sample bias voltage, one of these levels is lined up with the back-electrode states and a single electron can tunnel between the QD and back-electrode.

We can obtain the lever-arm, α, experimentally by fitting the observed spectrum with the theoretical one. Figures 6(b) and (c) show the results of the fitting. By assuming the temperature, we can extract the lever-arm, $\alpha = 0.04$. This means only 4% of the applied bias voltage is applied across the QD-back electrode tunnel barrier and 96% falls off across the tip–QD spacing. The converted energy in the QD is indicated as a scale bar in figure 5. Notice that as the temperature broadening becomes smaller at lower temperature, the oscillation amplitude needs to be reduced accordingly so that the peak shape is determined not by the tip oscillation but by the temperature.

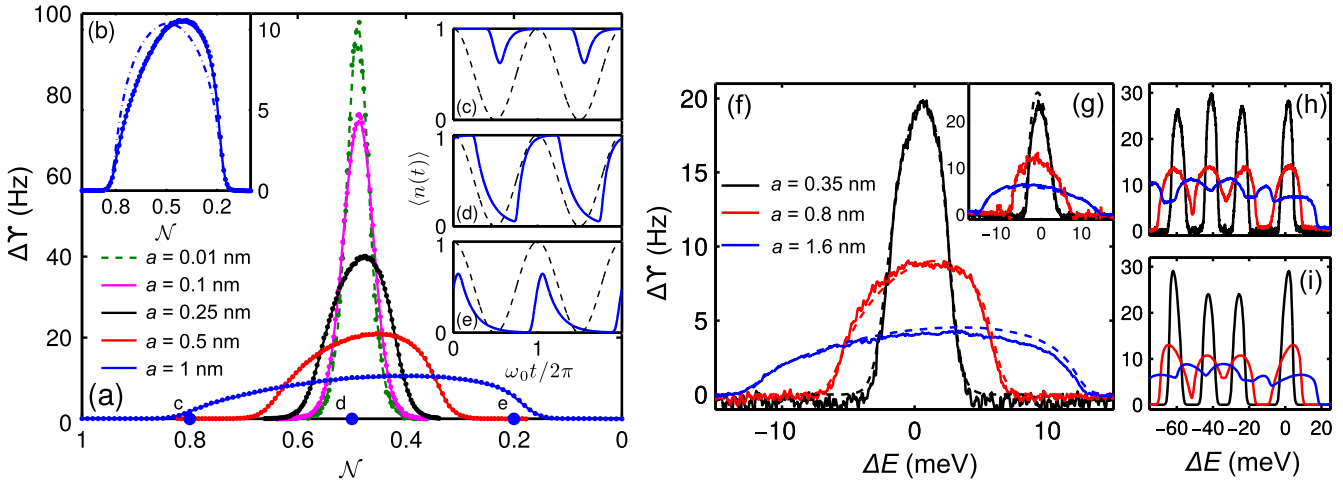

Figure 7. (a) Theoretical dissipation peak for $n = 1$ transition with different oscillation amplitudes. $\mathcal{N} = -V_B C_{tip}/e$ is the dimensionless bias voltage. Dotted (solid) lines are calculated from simulation (semianalytic theory). The green dashed line is from linear response. (b) Adiabatic approximation (dash-dotted), semianalytic theory (solid), and simulation (dot) for oscillation amplitude $a = 1$ nm. (c)–(e) Average dot charge versus time (solid) for $a = 1$ nm, at voltages marked in (a). Tip position is shown (thin dashed) as a reference. (f) Experimental (solid) and theoretical (dashed) dissipation peaks for $n = 1$ transition with three different oscillation amplitudes. (g) Dissipation peak for $n = 2$ transition. (h) Experimental dissipation peaks for the transitions in p-shell with three oscillation amplitudes. (i) Theoretical dissipation peaks calculated for the peaks in p-shell. Adapted with permission from [42]. Copyright (2010) by the American Physical Society.

We notice the larger peak separation between $n = 2$ and $n = 3$ peaks and between $n = 6$ and $n = 7$. It is indicative of the shell structure expected for 2D circularly symmetric potential that consists of lowest two-fold degenerate levels (s-shell, 2-spin × 1-orbital degeneracy) and the next lowest four-fold degenerate levels (p-shell, 2-spin × 2-orbital degeneracy). This type of shell structure has previously been observed for an ensemble of self-assembled InAs QD [34, 35]. Assuming this shell structure, we can obtain the charging energy from this peak separation between peak $n = 1$ and $n = 2$ as 30 meV using $\alpha = 0.04$ obtained before.

However, this simple argument to identify the shell structure is far from convincing. The more compelling identification usually requires the measurements under high magnetic field to acquire the evolution of energy level structure (Fock–Darwin spectrum) [6, 36]. In the next section, we will show an alternative way for the shell structure identification based on the asymmetry of the tunneling in and out processes.

4.1. Effect of degenerate levels on the dissipation peak

When the degeneracy of the energy levels in the QD is taken into account, the tunneling in and out process is no longer symmetric. Figure 6(a) illustrates the asymmetric tunneling process. When we consider the $n = 1$ peak in the spectrum shown in figure 6(b), the peak arises from the transition between $n = 0$ and $n = 1$ states. Assuming twofold spin degeneracy under no magnetic field, there are two ways for an electron to tunnel into the QD from the back-electrode, with either a spin-up or a spin-down, whereas there is only one way for the already occupied electron to tunnel out of the QD. For the $n = 2$ peak, the situation is opposite (one way to tunnel in, two ways to tunnel out). The same argument for the peaks in p-shell reveal the similar but more pronounced asymmetry for $n = 3$ and $n = 6$ peaks as illustrated in figure 6(a).

The effect of the asymmetric tunneling process manifests itself in two different ways depending on the tip oscillation amplitude. In the small oscillation amplitude case, the positions of the dissipation/frequency shift peaks shift with increasing temperature in the way that the peaks that belong to the same shell repel each other as indicated by arrows in figure 6(b). In the large oscillation amplitude case, the peaks that belong to the same shell get skewed away from each other as shown in figure 7.

4.1.1. Small tip oscillation amplitude case (Weak coupling).

In this case, we can obtain the analytical expression for the frequency shift and dissipation by considering the master equation and linear response theory [25, 37].

$$\Delta\omega = -\frac{\omega_0}{2k}\frac{A^2\Gamma^2}{k_B T}\frac{(n_{\text{shell}}+1)(\nu - n_{\text{shell}})}{\omega^2 + (\phi\Gamma)^2} f(\Delta E)[1 - f(\Delta E)] \tag{9}$$

$$\Delta\gamma = \frac{\omega_0^2 A^2 \Gamma}{k k_B T}\frac{(n_{\text{shell}}+1)(\nu - n_{\text{shell}})}{\omega^2 + (\phi\Gamma)^2} f(\Delta E)[1 - f(\Delta E)] \tag{10}$$

where n_{shell} is the number of electrons already in the shell before adding a new electron, ν level degeneracy and $\phi = (\nu - n_{\text{shell}})f + (n_{\text{shell}} + 1)(1 - f)$. While these results indicate the deviation of the peak shape from the simple form of $4\cosh^{-2}(\Delta E/2) = f(\Delta E)(1 - f(\Delta E))$, which reflects the asymmetry of the tunneling process, the deviation is too small to be discernible. Instead, each peak position changes with temperature in its own unique way from which the level degeneracy can be identified.

Figures 6(b) and (c) show the direction of the peak shift of each peak for increasing temperature and the temperature

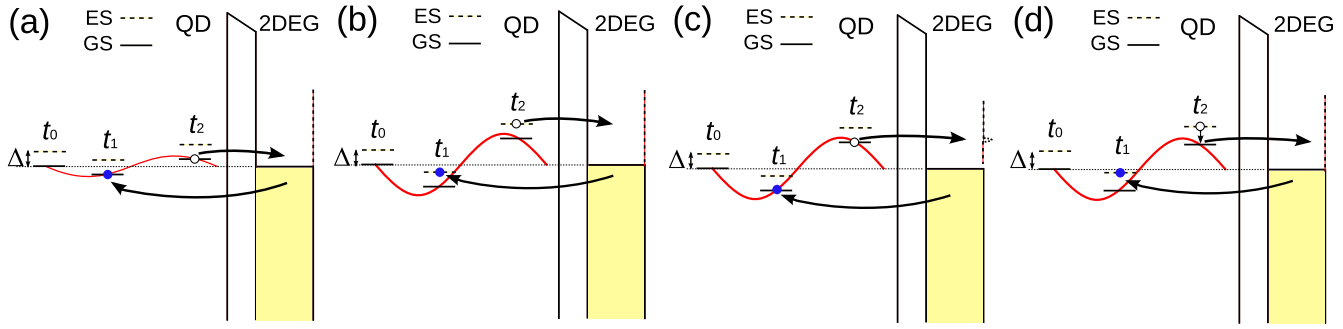

Figure 8. The oscillating AFM tip (symbolized by the red curve), modulates the QD levels around. The levels are shown at three separate times, t_0 is the initial position of the levels, at t_1 and electron tunnels into the dot, and at t_2 an electron tunnels out of the dot. The filled states of the 2DEG are shown in yellow. (a) A small oscillation amplitude opens an energy window that just allows tunneling into the ground state (GS). (b) The larger oscillation amplitude opens an energy window that allows tunneling into the first excited state (ES) as well as GS (Δ: energy level spacing). (c) The energy window touches a region where the density of states of the 2DEG is not uniform, affecting the tunneling rate of the tunneling-out electron. (d) Inelastic tunneling process involving photon/phonon emission. Reprinted with permission from [46]. Copyright (2012) American Chemical Society.

dependence of $n = 1$ and $n = 2$ peaks, respectively. The peak shift is linearly proportional to the temperature and the level degeneracy can be inferred from the slope of the peak shift versus temperature line. Although a similar effect has been predicated for the current transport measurements in SETs [38, 39], it has rarely been observed experimentally [40, 41]. The peak shift observed in the dissipation measurement is much more clear because the effect appearing in the dissipation peak is much more pronounced compared with the conductance peak as predicted by theory [25].

4.1.2. Large tip oscillation amplitude case (Strong coupling).

In the large tip oscillation case, the effect of degeneracy appears as an asymmetric peak shape that is much more pronounced and thus clearly observable than in the small oscillation amplitude case. This makes it possible to identify the shell structure by sweeping V_B with a large tip oscillation amplitude than measuring the more challenging temperature dependence of the peak position described above. The large oscillation amplitude refers to the case where the maximum change in the energy detuning due to the oscillator, $\Delta E_{osc} = Aa$ (a: oscillation amplitude), is comparable to thermal energy, $k_B T$. In this case, the tunneling rates depend nonlineary on the tip position, z and the master equation needs to be numerically solved to obtain $\langle n(t)\rangle$. The expressions for frequency shift and dissipation can be obtained using the theory of FM-AFM [43, 44] as shown below:

$$\Delta\omega = -\frac{\omega_0^2}{2\pi ka}\int_0^{2\pi/\omega_0} F_{dot}(t)\cos(\omega_0 t)\,dt = -\frac{\omega_0^2 A}{2\pi ka}\int_0^{2\pi/\omega_0} \langle n(t)\rangle \cos(\omega_0 t)\,dt \quad (11)$$

$$\Delta\gamma = \frac{\omega_0^2}{\pi ka}\int_0^{2\pi/\omega_0} F_{dot}(t)\sin(\omega_0 t)\,dt = \frac{\omega_0^2 A}{\pi ka}\int_0^{2\pi/\omega_0} \langle n(t)\rangle \sin(\omega_0 t)\,dt \quad (12)$$

equations (11) and (12) can also be derived from a more quantum mechanical approach [45].

Figure 7 shows the theoretical ((a)–(e)) and experimental ((f)–(g)) dissipation versus bias voltage spectra for the $n = 1$ transition with different tip oscillation amplitudes. The theoretical curves are obtained from equation (12) using $\langle n\rangle$ calculated from the master equation numerically. Figures 7(c)–(e) show the time evolution of $\langle n\rangle$ calculated for different bias positions. We notice that $\langle n(t)\rangle$ is no longer sinusoidal and that the dissipation peaks become wider and get more skewed towards the direction of $n = 0$ state for larger amplitude. The skewed peak stems from the asymmetric tunneling process we described above (figure 6(a)). Figures 7(f)–(i) show the excellent agreement between the theory and experiments. All the theoretical curves are calculated using the following parameters, $2E_C = 31$ meV, $\alpha = 0.04$, and $\Gamma = 70$, 90 kHz for peaks $n = 1$ (figure 7(f)) and $n = 2$ (figure 7(g)), all of which are obtained from the experimental results taken at weak coupling conditions (small oscillation amplitude), only A being a fitting parameter. The tip oscillation amplitude, a, is obtained from the calibrated interferometer signal. The peaks shown in figure 7(g) corresponds to the $n = 2$ transition and is skewed in the opposite direction as $n = 1$ peak because of the opposite asymmetry of the tunneling process. Figures 7(h) and (i) show the experimental and theoretical dissipation peaks versus voltage for the peaks belonging to the p-shell, respectively. The excellent agreement between the theory and the experiment also demonstrates the validity of the theoretical interpretation. In summary, by finding a pair of peaks which are skewed away from each other, the shell-filling can be identified without measuring magnetic field or temperature dependence of the spectra.

4.2. Excited-states spectroscopy with a large oscillation amplitude

The analysis in the previous section suggests the possibility of probing the excited states of the QDs by taking the dissipation spectra with large oscillation amplitudes. When the tip motion

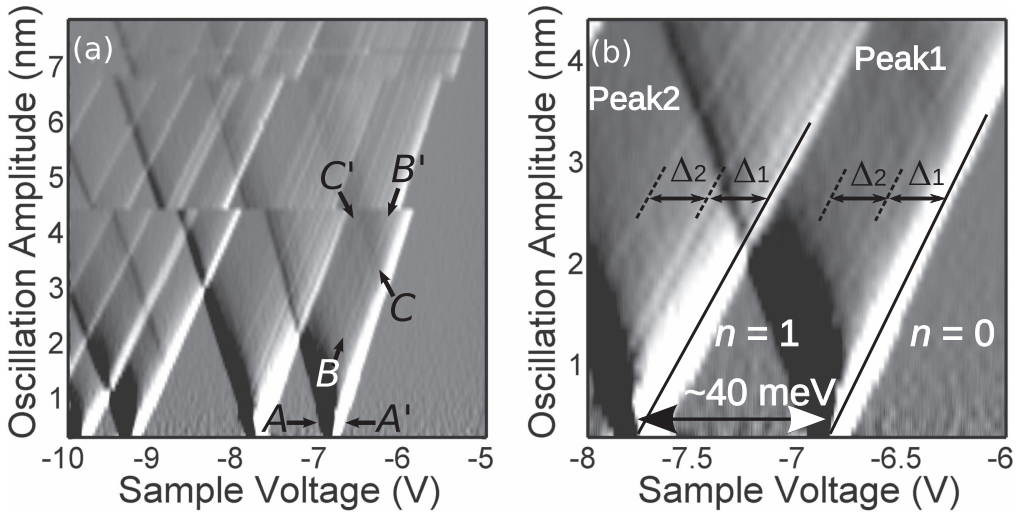

Figure 9. (a) Derivative of dissipation versus bias voltage curves taken at different oscillation amplitudes. (b) Zoom-up of the region around A and A' indicated in (a). Reprinted with permission from [46]. Copyright (2012) American Chemical Society.

is large enough, the energy detuning (bias window) modulated by the tip motion becomes large enough to allow the tunneling to the excited states (figure 8(b)). This situation is illustrated in figure 8. This additional tunneling paths to the excited states show up as additional features in damping versus voltage spectra. Figure 9 shows such experimental results [46]. The figure consists of the derivatives of 67 dissipation versus voltage spectra taken with different tip oscillation amplitudes.

The down-pointing triangles in the figure are equivalent to the Coulomb diamonds commonly observed in the current transport spectroscopy experiments where the vertical axis is the source–drain bias voltage of a single electron transistor (SET) in place of the oscillation amplitude. The lines that run parallel to the rightmost triangle edges (e.g.,*B*-*B*′) in figure 9(a) result from the opening of additional tunneling paths which become available in the tunnel bias window. In this case, the bias window is set by the lowest and highest energy detuning each of which is determined by the closest and furthest position of the tip. The technique allows us to probe directly the excitation spectrum of the QDs for a fixed number of electron without optical measurement and can thus be applied to measure spin-excitation energy under magnetic field which is important for single electronic spin manipulations [2]. The additional tunneling paths can also be due to inelastic tunneling or features in the density of states of the back-electrode [47]. Ability to probe excited states directly can be applied to such interesting applications as inelastic tunneling spectroscopy [48, 49] or single-electron spin detection [2].

4.3. Spatial mapping of charging on strongly interacting QD–Charge stability diagram

As we have already seen in the section 2.4, e-EFM is capable of obtaining spatial maps of single-electron charging events in the QD. Figure 10 shows such an example. Figure 10(a) is the topography image of an InAs island and (b) is the dissipation image taken at the same location with $V_B = -8.0$ V. While the topography shows one connected island, the dissipation image shows at least two sets of concentric rings, indicating the existence of multiple QDs in the island.

Although the current transport spectroscopy on a single QD has been performed on InAs QDs by attaching a pair of electrodes with a nanogap [50], it would not be straightforward to identify such multiple dots just with the conventional conductance versus bias voltage spectra. The similar spatial maps showing concentric rings have been observed by a related technique, scanning gate microscopy (SGM) [20, 51–54]. In SGM, the AFM tip is used just as a movable gate and the conductance of QD devices is measured as a function of the tip position. While SGM is more widely used to investigate the properties of individual QDs, it still requires the fabrication of the wired QD devices.

Figure 10(c) is the zoom-up of the lower left corner of figure 10(b). Overall, the image resembles the charge stability diagram of double QD systems. The image shows two set of rings which avoid each other. These avoided crossings are indicative of the coupling between two QDs. More detailed analysis of the avoided crossing can quantitatively reveal the nature of the coupling, either capacitive or quantum mechanical (tunnel) [55], which is of critical importance for quantum information processing application.

Figure 11 shows that a set of concentric rings shown in figure 11(b) can be converted to a conventional charge stability diagram. Figure 11(c) can be obtained by the coordinate transformation, $(x, y) \rightarrow (V_U, V_L)$ where V_U and V_L are equivalent bias for the upper and left QDs. In this particular case, we use the experimentally obtained relations, $V_U = \beta_U\sqrt{(x - x_U)^2 + (y - y_U)^2}$ and $V_L = \beta_L\sqrt{(x - x_L)^2 + (y - y_L)^2}$ where (x_U, y_U) and (x_L, y_L) are the center of each QD, β_U and β_L are constants which can be obtained by measuring the radius of each ring at different bias voltages, V_B.

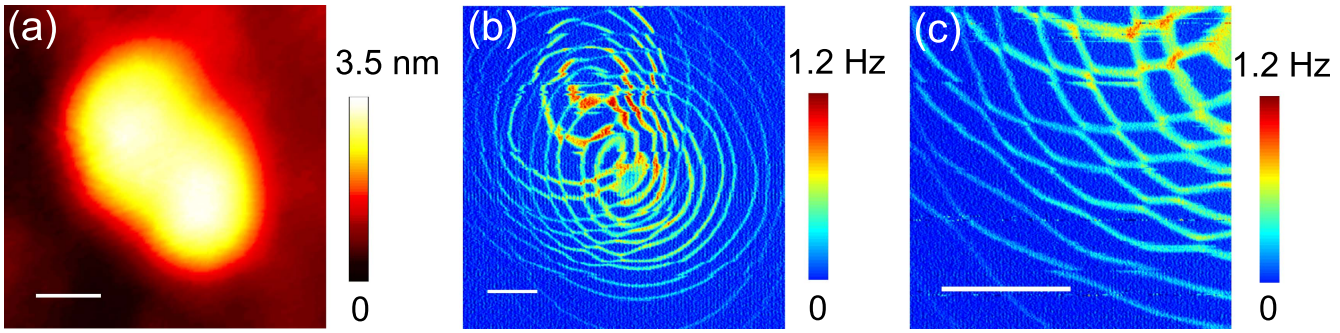

Figure 10. (a) AFM topography of an InAs QD island. (b) dissipation images of InAs QD taken at $V_B = -8.0$ V. (c) Zoom up of the lower left corner of the image (b) showing many avoided crossings [25]. Scale bar is 20 nm.

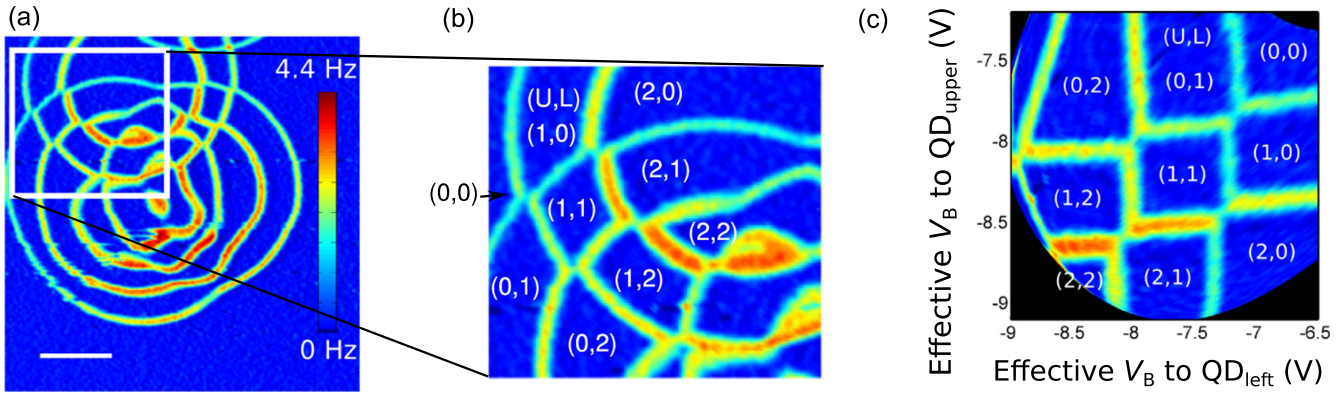

Figure 11. (a) Dissipation image of the same QD as that in figure 10 taken with $V_B = -8.0$ V at a larger tip–QD distance. Scale bar is 20 nm. (b) Zoom-up of (a). (c) Charge stability diagram obtained from (b) by coordinate transformation. Vertical axis and horizontal axis are effective bias voltage applied to the upper and left QD, respectively. The two numbers in parenthesis in (b) and (c) indicate the number of electrons in the upper and left QDs.

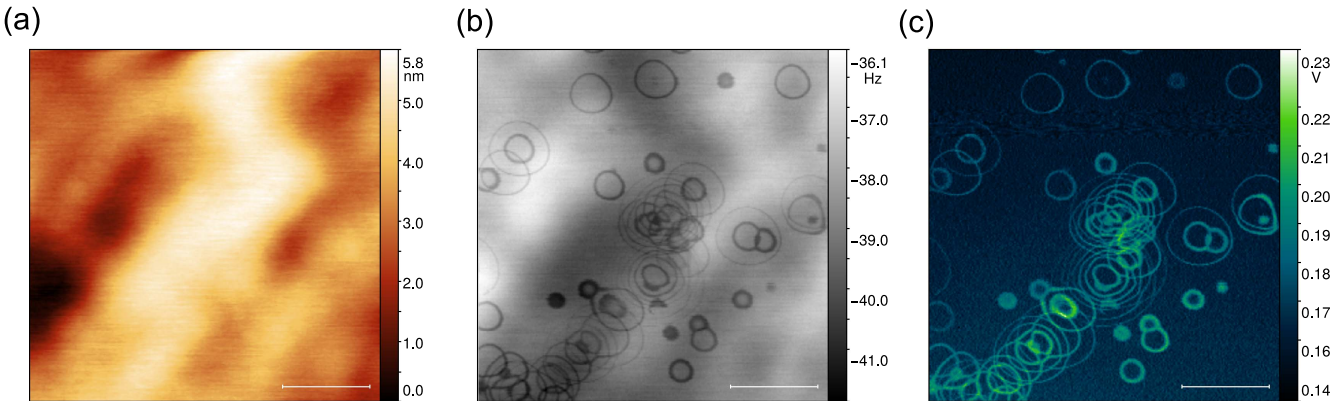

Figure 12. (a) Frequency modulation mode AFM topography, (b) frequency shift and (c) dissipation images of of the same location of a capped InAs QD grown on InP taken at $T = 4.5$ K. Scale bar is 1 μm. The topography image was taken separately. The frequency shift and dissipationimages were taken simultaneously in constant height mode.

4.4. Imaging of capped QD

For practical device applications such as QD lasers, epitaxially grown semiconductor QDs are usually covered with a protecting layer [56] or even buried in the host matrix to prevent them from being oxidized. As e-EFM technique relies on the detection of long-range electrostatic force, it can be used to probe the capped or buried QDs. Figure 12 shows the topography, frequency shift and dissipation images of the InAs QD capped with a thin layer of InP. The topography image is taken with FM mode and the frequency shift and dissipation images are simultaneously taken in constant height mode. While the topography of the QDs is much less obvious than uncapped QDs, the charging rings appear very clearly in frequency shift and dissipation images. The background in the frequency shift image originates from the topography through the third term of the expression of the electrostatic force in equation (2). This demonstrates a clear advantage of the e-EFM technique over tunneling

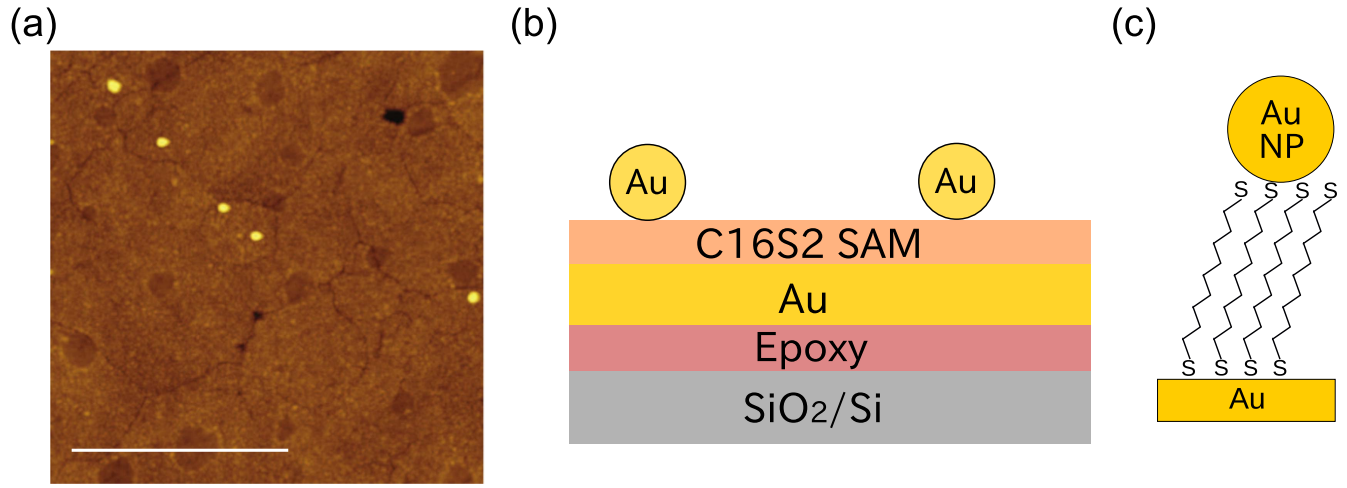

Figure 13. (a) AFM topography images of 5 nm diameter Au nanoparticles (five bright spots) on C16S2 SAM. Scale bar is 500 nm. (b) Schematic of the cross sectional view of the sample. (c) Schematic of Au NP -C16S2–Au substrate structure.

spectroscopy by STM which requires a clean surface to ensure a reliable vacuum tunnel gap [57].

5. Colloidal Au NPs on alkane-dithiol self-assembled monolayer (SAM)

QDs based on colloidal NPs have been attracting considerable attention because of their tunable optoelectronic properties by their size and constituent material. The capability of producing a wide variety of NPs with different materials, shapes and sizes together with the possibility of arranging them and integrating them with other structures has a huge potential for various applications [58]. Investigating the electronic structure of individual colloidal QDs have been of great importance in order to uncover the relationship between their electronic and geometric structures and also to engineer more complex structure based on colloidal QDs. Scanning tunneling microscopy and spectroscopy (STM and STS) have been so far used to this end [23]. Although the conductance spectroscopy in SET with NP as an island have also been performed [59–61], the device fabrication remains challenging.

We apply e-EFM technique to study the single-electron charging in colloidal bare gold nanoparticles (Au NPs). For this study, the sample as shown in figure 13(b) has been prepared. The SAM of 1,16-hexadecanedithiol (C16S2) is formed on a template strip gold surface and is used as a tunnel barrier. Bare Au NPs with 5 nm diameter are deposited on the C16S2 SAM layer to form a Au NP-C16S2-Au junction (figure 13(c)). Figure 13(a) shows the AFM topography image of the prepared sample. Covalent Au-S bonds form stable links between Au NPs and Au substrate through alkyl chains that act as a tunnel barrier [62, 63]. The alkanedithiol SAM is ideally suited to optimize the tunnel barrier so that the tunneling rate matches the oscillation frequency of the AFM cantilever.

Figure 14(a) shows a typical dissipation versus bias voltage curve taken above a 5 nm Au NP on the sample at the temperature of 4.5 K. A set of very sharp single-electron charging peaks are clearly seen in the figure. The equal separations between the neighboring peaks indicate that the Au NP is in the classical Coulomb blockade regime ($\delta \ll k_B T \ll E_C$), which is consistent with the expected $\delta \approx 1$ meV estimated for 5 nm Au NPs [64]. The inset shows the zoom up of the rightmost peak together with the fitted curve (blue line) with the function, $\cosh^{-2}[e\alpha(V_B - V_0)/2k_B T]$ from which $\alpha = 0.0054$ is extracted. Using the extracted α value, the charging energy of the Au NP is obtained as $E_C = 16$ meV.

Figures 14(b)–(g) show the spatial mapping results on a Au NP. The top and bottom panel shows the result at 77 K and 4.5 K, respectively. The concentric rings due to the single-electron charging can be clearly seen even at 77 K but the contrast of the ring to the background is much higher at 4.5 K. As is shown here, e-EFM technique can be used to investigate the NP complex as those demonstrated in [7–9].

5.1. Revealing density-of-states from tunneling-rate spectrum

The expressions for $\Delta\omega$ and $\Delta\gamma$ given in equations (6) and (7) are derived for a single non-degenerate level, in which case the total tunneling rate, $\Gamma_\Sigma = \Gamma_+ + \Gamma_-$, is constant and equal to the tunnel coupling constant. In general, the tunneling rate depends on the energy level structure and is thus energy dependent. The corresponding results for generic energy-dependent tunneling rate in the limit of weak coupling (small oscillation amplitude) are obtained as follows [37]:

$$\Delta\omega = -\frac{\omega_0 A^2}{2k}\frac{(\Gamma'_+\Gamma_\Sigma - \Gamma_+\Gamma'_\Sigma)}{(\Gamma_\Sigma^2 + \omega^2)} \tag{13}$$

$$\Delta\gamma = \frac{\omega_0^2 A^2}{k\Gamma_\Sigma}\frac{(\Gamma'_+\Gamma_\Sigma - \Gamma_+\Gamma'_\Sigma)}{(\Gamma_\Sigma^2 + \omega^2)} \tag{14}$$

where $'$ denotes derivative with respect to energy. The total tunneling rate between the QD and the back-electrode, Γ_Σ, can be directly measured as a function of the electrochemical potential detuning by noting that:

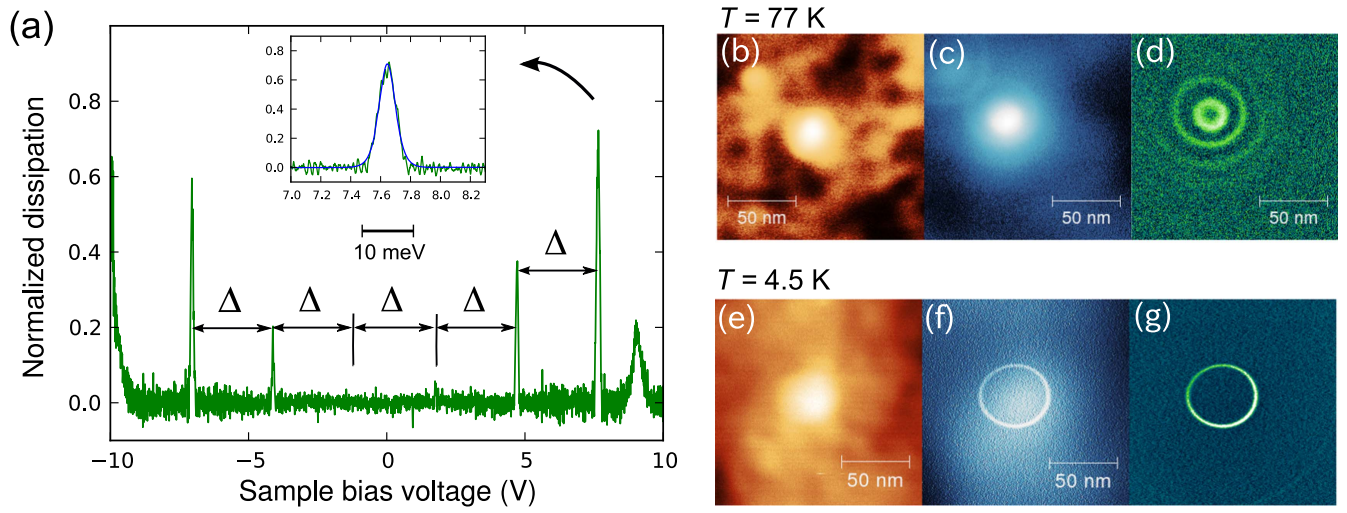

Figure 14. (a) Dissipation Spectrum on Au NP taken at $T = 4.5$ K. The energy scale in the QD is indicated as a scale bar (10 meV). (Inset) Blue solid curve is a fitted curve with the theory. (b) and (e) Topography, (c) and (f) frequency shift, (d) and (g) dissipation images on Au NP taken at 77 K and 4.5 K, respectively.

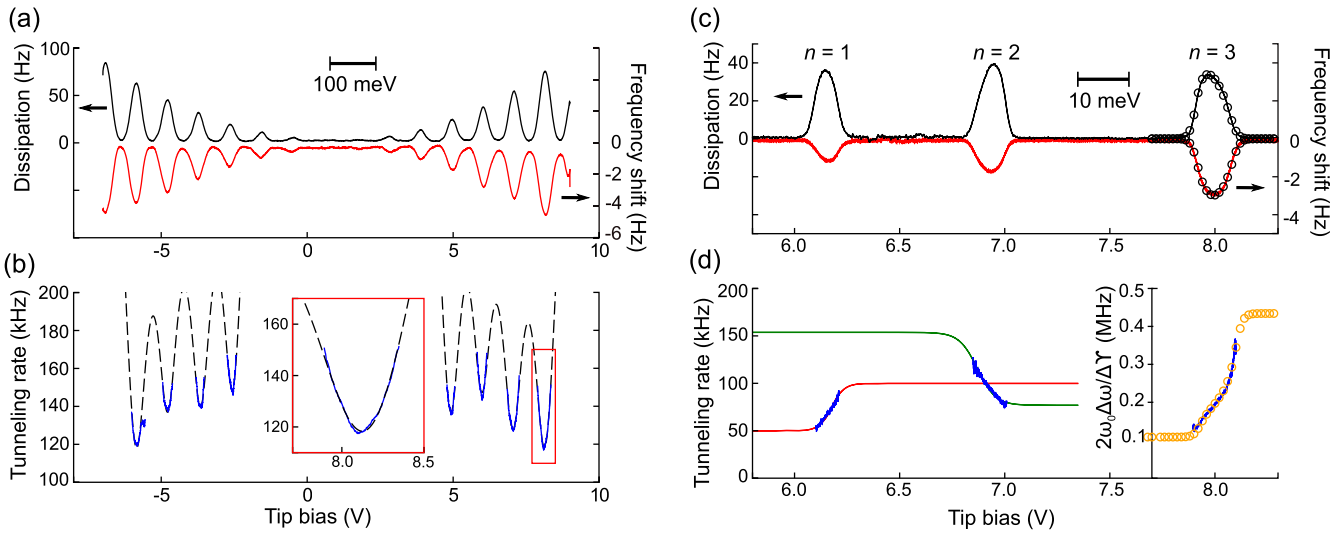

Figure 15. Effect of density-of-states on tunneling rate. (a) Experimental frequency shift and dissipation versus bias voltage curves measured on Au NP at 77 K. The energy scale in the Au NP is indicated as a scale bar (100 meV) determined from the lever-arm, $a = 0.064$. (b) Extracted tunneling rate from the data above using equation (15) (blue solid line). Dashed line is a fit to the analytical expression for a continuous density of states. (c) Experimental frequency shift and dissipation versus bias voltage curves measured on InAs QD at 4 K. The energy scale in the QD is indicated as a scale bar (10 meV) determined from the lever-arm, $a = 0.04$. (d) Corresponding tunneling rate data (blue) obtained from the data above. Green and blue solid lines are fits to the tunneling rate expected for 2-fold degenerate levels. Circles represent a best fit solution assuming tunneling into an empty 4-fold degenerate level accounting for the strong coupling effect. Adapted with permission from [37]. Copyright (2015) American Chemical Society.

$$\Gamma_{\Sigma}(\Delta E) = -2\omega_0 \frac{\Delta\omega}{\Delta\gamma}. \tag{15}$$

This points to the interesting possibility of tunneling-rate spectroscopy from which the energy level structure (density-of-states) of the QD can be extracted. It should be noted that the measuring the tunneling rate with current spectroscopy measurement in SET is not as straightforward because two tunnel barriers are involved. Alternative single-electron counting techniques require fast charge sensors [65].

Figure 15 shows three examples of such tunneling-rate spectroscopy using e-EFM. Figure 15(b) shows energy dependent tunneling rate for a Au NP which is obtained from the $\Delta\omega$ and $\Delta\gamma$ spectra shown in figure 15(a). A parabola like energy dependent tunneling rate (blue curve) is clearly seen in the spectrum which is fitted with the energy dependent tunneling rate expected for the continuous density of states (dashed line) [26, 38]. Figure 15(c) shows the experimental frequency shift and dissipation spectra measured on InAs QD at 4.5 K. (similar to the result in figure 5 but the bias axis is reversed). Three peaks for $n = 1$, $n = 2$ and $n = 3$ are seen from left to right. Figure 15(d) shows the corresponding tunneling rate spectra for each peak (blue line). The green and red lines are fits with the the theoretical tunneling rate expression expected for 2-fold degenerate levels with the

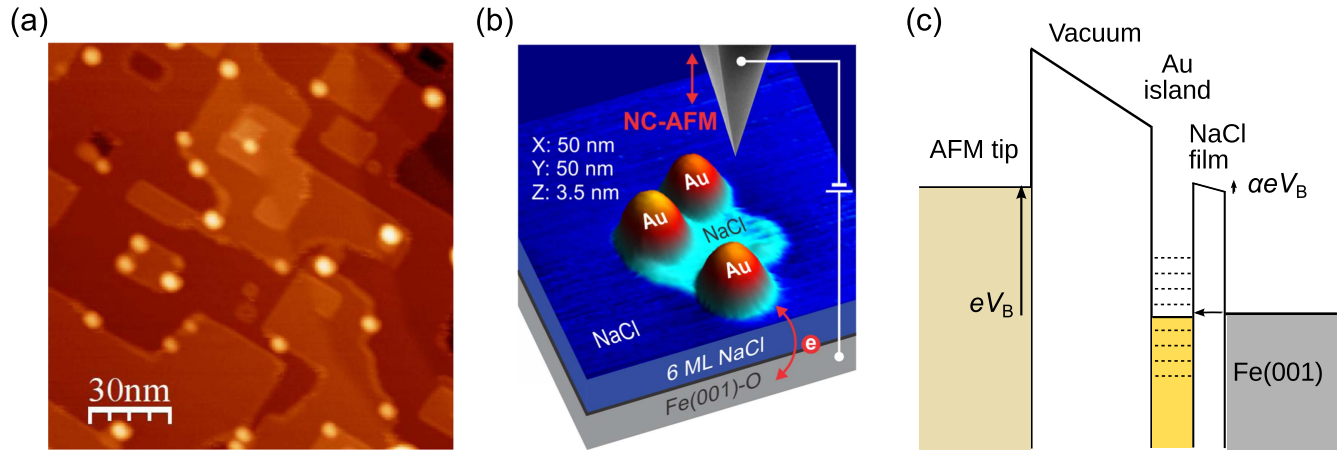

Figure 16. (a) Frequency modulation mode AFM topography of Au islands on 7 ML thick NaCl. (b) Schematic diagram of the experimental setup. (c) Energy level diagram of the system. Adapted with permission from [27]. Copyright (2012) American Chemical Society.

shell-filling, $n_{\text{shell}} = 0$ and $n_{\text{shell}} = 1$, respectively. The yellow circle is a fit to the theory for 4-fold degenerate levels with $n_{\text{shell}} = 0$. We can clearly see the asymmetric tunneling processes which are discussed in section 4.1 in the tunneling rate spectra although it is not obvious at all to identify them in the charging peaks in either frequency shift or dissipation spectrum. In other words, it is possible to identify the shell filling from the slope of the tunneling rate spectra. This approach can be extended to identify more general energy level structures [37].

6. Au island on a few monolayer thick NaCl grown on Fe(001) surface

The charge transfer process to metallic islands on insulator surfaces have been the subject of active research particularly in the context of supported model catalysts [66]. STM has been a main tool for investigating the relationship between the size and shape of individual islands and their electronic properties including charge transfer [67]. However, as STM requires a dc current typically higher than 1 pA, it can only be applied to systems of a few monolayers of insulators. Here, we demonstrate that e-EFM technique can be applied to the gold islands deposited onto thicker insulating films.

Figure 16(a) shows the AFM topography image of the sample with a 7 ML thick NaCl grown on a Fe(001) surface with a submonolayer coverage of Au. The NaCl layer grows in a nearly perfect layer-by-layer growth mode [68], allowing for the tunneling rate to be controlled. Figures 16(b) and (c) show the schematic and the energy level diagram of the experimental setup. The size of the studied Au nanoislands is 3.5 nm in height and 10 nm in apparent diameter which is likely to be larger than the actual dimension of the QDs due to tip convolution effects.

Figure 17(b) shows the dissipation image taken over the three Au islands shown in figure 17(a) with the tip height of 7.5 nm and $V_B = 10$V. The measurements were performed at room temperature under ultra-high vacuum condition. A circular ring with a dot at its center appear for each of the islands, indicating single-electron tunneling between the Au islands and Fe(100) back-electrode through 7 ML NaCl film [27]. Figure 17(c) is the dissipation versus bias voltage spectrum taken at the center of one of the three islands (indicated by $\times$). We can see three single-electron charging peaks whose separations are roughly equal. Fitting the peaks with $\cosh^{-2}[e\alpha(V_B - V_0)/2k_BT]$ provides $\alpha = 0.04$ by which the addition energy of 137 $\pm$ 27 meV can be obtained. By taking this value as the charging energy of the Au island (assuming the negligible contribution of the quantum confinement energy), we can determine the shape of the Au island as a truncated sphere with the base diameter of 4.2 nm from the finite-element electrostatic modeling of the system using the measured height of the island. Similar charging peaks are observed in the frequency shift versus bias voltage spectrum as well, enabling the determination of the electron tunneling rate through NaCl layer ranging from 61 to 285 kHz for the three peaks.

The approach presented in this section can be applied to a variety of interesting systems such as metallic islands on oxide films that are widely studied model catalysts. The interaction of even smaller islands with molecules could be investigated by monitoring the electronic level structure of these islands with the technique discussed above.

7. Possible application to other systems

The application of e-EFM technique is not limited to QDs. SETs incorporating individual molecules have been studied actively in recent years [48], and different charge states of single molecules have been observed in conductance spectroscopy [69–71]. We can therefore imagine that e-EFM can be applied to investigate the properties of single molecules. As the fabrication of single-molecule SETs is inherently challenging [72] because a single molecule cannot be placed in the nanogap electrodes in a well controlled manner, e-EFM could be used as a new technique to investigate the electronic energy levels of individual molecules that interact with a substrate [71].

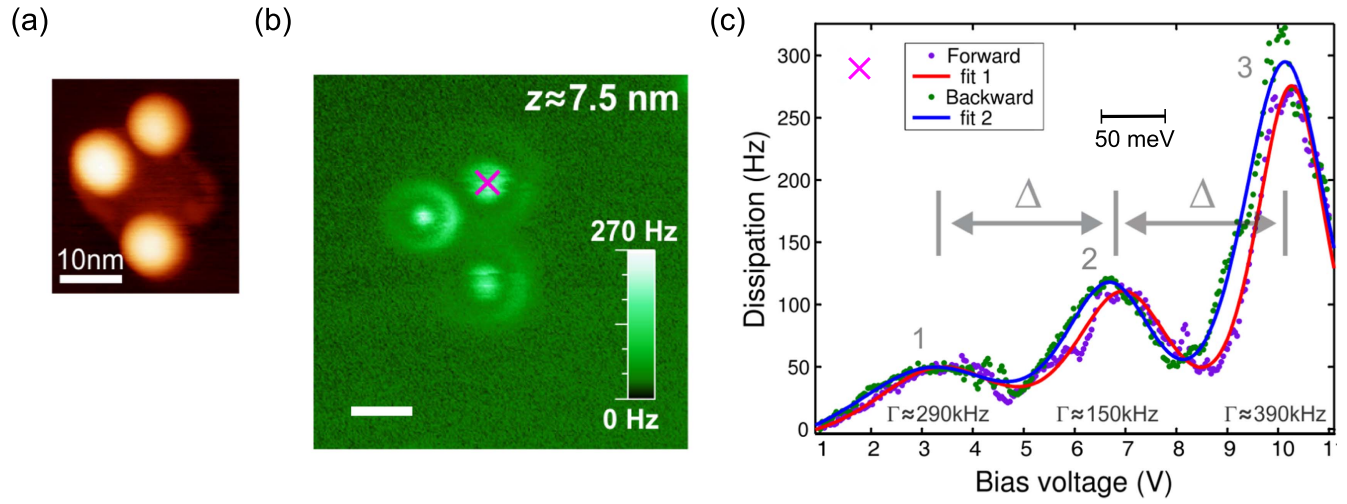

Figure 17. (a) Frequency modulation mode AFM topography image of Au islands on 7 ML thick NaCl. The height of the islands is 3.5 nm. (b) Dissipation image on the same Au islands taken at $V_B = 10$ V and $a = 1$ nm. (c) Dissipation versus V_B curve taken on the Au island indicated as× in (a). The energy scale in the Au NP is indicated as a scale bar (50 meV) determined from the lever-arm, $\alpha = 0.04$. Adapted with permission from [27]. Copyright (2012) American Chemical Society.

Another interesting system for e-EFM technique is individual dopant atoms in semiconductors. While the behavior of individual dopant atoms is becoming increasingly important in ever shrinking semiconductor electronic devices, these individual dopants are emerging as a new class of quantum mechanical entities whose discrete energy levels can be used for applications in quantum information processing such as qubits and non-classical light sources [73]. Although spectroscopy of individual dopants can be performed in a SET geometry [74, 75], STM has also been applied to detect the charge state of individual dopant by detecting the electron tunneling through bound states due to the dopant atoms [76]. In addition to the advantage of STM based experiments which do not require the fabrication of device, e-EFM can be applied to the dopants that are much more weakly coupled to the bulk states as the required tunneling rate to observe a signal is much lower than that for STM (recall that 1nA corresponds to 10^{10} electrons per second).

8. Relation to other techniques

The e-EFM technique shares several common features with capacitance/admittance spectroscopy. Single-electron tunneling spectroscopy has been performed with capacitance spectroscopy technique [34, 77]. In capacitance spectroscopy, a QD is connected to a lead through a tunnel barrier and the charge in the QD is controlled by a gate voltage. Single-electron tunneling is induced by applying an ac voltage to the gate and the resulting ac current is measured by a lock-in amplifier. Although the capacitance spectroscopy has successfully been applied to gate-defined QDs [16, 77, 78], it has not been widely adapted for individual QDs because of the difficulty in detecting the weak electrical signal from single-electron tunneling. Recently, similar measurements using RF resonators have emerged as an alternative technique to current transport spectroscopy for probing the quantum states of QDs. In this scheme, an RF resonator is directly coupled to the QD through either a source/drain electrode [11, 79–82] or a gate electrode [13, 83–86] and the changes in the phase and amplitude of the reflected RF signal due to the single-electron tunneling are detected (RF reflectometry). The changes in the phase and dissipated power of the microwave signal are expressed for small RF excitation limit as follows:

$$\Delta\phi \simeq -\frac{\pi Q_{\rm res}}{C_{\rm p}}\frac{(e\alpha)^2}{2k_{\rm B}T}\frac{1}{1+(\omega_0/\Gamma)^2}f(\Delta E)[1-f(\Delta E)] \tag{16}$$

$$\Delta P \simeq \frac{(e\alpha V_{\rm g}^{\rm rf})^2}{2k_{\rm B}T}\frac{\omega_0/\Gamma}{1+(\omega_0/\Gamma)^2}f(\Delta E)[1-f(\Delta E)] \tag{17}$$

where $Q_{\rm res}$ is the quality factor of the RF resonator, $C_{\rm p}$ the paracitic capacitance, α is the lever-arm, $\alpha = C_{\rm g}/C_\Sigma$, $V_{\rm g}^{\rm rf}$ the RF signal excitation amplitude [84].

This technique is emerging as a promising way to detect the charge state of QDs which is indispensable for readout of the qubits based on QDs. e-EFM can be considered as a mechanical analog of this technique. In e-EFM, a mechanical resonator (AFM cantilever) is capacitively coupled to the QDs in place of an RF resonator and its response to the change in charge state is detected as the changes in resonance frequency and dissipation, similarly to the RF admittance measurements. Therefore, admittance spectroscopy should be able to measure shell-filling (sections 4.1.1 and 4.1.2), perform excited-states spectroscopy (section 4.2) and determine density-of-states (section 5.1) in complete analogy to our e-EFM measurements. Although RF reflectometry techniques have been applied for other systems than gate-defined QDs such as single dopants [82, 83] or NPs [86], the devices which incorporate dopants or NPs still need to be fabricated. Along with the topographic imaging capability, e-EFM can be a powerful tool for exploring new nanoscale material systems such as single molecules, NP complexes as possible quantum bits.

9. Conclusion

We demonstrated that charge sensing by electrostatic force microscopy is capable of quantitative electronic energy level spectroscopy of QDs in three distinct systems, epitaxially grown InAs self-assembled QDs on InP, colloidal Au nanoparticles on alkanedithiol self-assembled monolayer and Au nanoislands deposited on NaCl.

Three different methods for probing the energy level structure of QDs are demonstrated. The direction of the temperature-dependent shift of the charging peaks in the small tip oscillation case (section 4.1.1) and the direction of the skewness of the peaks in the large tip oscillation case (section 4.1.2) enable straightforward identification of shell-filling of QDs. The energy-dependent tunneling rate which can easily be obtained by e-EFM offers more general approach to probe energy level structure of the QDs. Excited-states spectroscopy is also possible by measuring the tip oscillation amplitude dependence of the single-electron charging spectra. All the features described above makes e-EFM a powerful technique for readout of the charge state of QDs.

The spatial mapping capability of the e-EFM technique provides a new route for the research on unconventional QDs such as multi-QDs based on NPs, individual molecules, dopants and defects. In combination with topographic imaging and structural characterization capabilities of AFM, e-EFM will play an important role in searching for new device elements for nanoelectronics including qubits.

Acknowledgments

We thank P Poole, S Studenikin, and A Sachrajda at the National Research Council of Canada for providing the InAs QD sample and for fruitful discussion, L Cockins and A Tekiel for their experimental contributions, A A Clerk and S D Bennette for their theoretical contributions. This work was supported by funding from NSERC and FQRNT.

References

[1] Elzerman J M, Hanson R, van Beveren L H W, Witkamp B, Vandersypen L M K and Kouwenhoven L P 2004 Single-shot read-out of an individual electron spin in a quantum dot *Nature* **430** 431–5

[2] Elzerman J M, Hanson R, van Beveren L H W, Tarucha S, Vandersypen L M K and Kouwenhoven L P 2005 Semiconductor few-electron quantum dots as spin qubits *Quantum Dots: A Doorway to Nanoscale Physics* ed H-D Wiemhöfer (Berlin: Springer) pp 25–95

[3] Petta J R, Johnson A C, Taylor J M, Laird E A, Yacoby A, Lukin M D, Marcus C M, Hanson M P and Gossard A C 2005 Coherent manipulation of coupled electron spins in semiconductor quantum dots *Science* **309** 2180–4

[4] Gorman J, Hasko D G and Williams D A 2005 Charge-qubit operation of an isolated double quantum dot *Phys. Rev. Lett.* **95** 090502

[5] Fulton T A and Dolan G J 1987 Observation of single-electron charging effects in small tunnel junctions *Phys. Rev. Lett.* **59** 109–12

[6] Kouwenhoven L P, Austing D G and Tarucha S 2001 Few-electron quantum dots *Rep. Prog. Phys.* **64** 701–36

[7] Milliron D J, Hughes S M, Cui Y and Manna L 2004 Colloidal nanocrystal heterostructures with linear and branched topology *Nature* **430** 190–5

[8] Aldaye F A and Sleiman H F 2007 Dynamic DNA templates for discrete gold nanoparticle assemblies: control of geometry, modularity, write/erase and structural switching *J. Am. Chem. Soc.* **129** 4130–1

[9] Chen Y-S, Hong M-Y and Huang G S 2012 A protein transistor made of an antibody molecule and two gold nanoparticles *Nat. Nanotechnol.* **7** 197–203

[10] Schönenberger C and Alvarado S F 1990 Observation of single charge carriers by force microscopy *Phys. Rev. Lett.* **65** 3162–4

[11] Petersson K D, Smith C G, Anderson D, Atkinson P, Jones G A C and Ritchie D A 2010 Charge and spin state readout of a double quantum dot coupled to a resonator *Nano Lett.* **10** 2789–93

[12] Petersson K D, McFaul L W, Schroer M D, Jung M, Taylor J M, Houck A A and Petta J R 2012 Circuit quantum electrodynamics with a spin qubit *Nature* **490** 380–3

[13] Colless J I, Mahoney A C, Hornibrook J M, Doherty A C, Lu H, Gossard A C and Reilly D J 2013 Dispersive readout of a few-electron double quantum dot with fast rf gate sensors *Phys. Rev. Lett.* **110** 046805

[14] Clerk A A and Bennett S 2005 Quantum nanoelectromechanics with electrons, quasi-particles and Cooper pairs: effective bath descriptions and strong feedback effects *New J. Phys.* **7** 238

[15] Wasshuber C 2001 Computational single-electronics *Computational Microelectronics* (Vienna: Springer)

[16] Ashoori R 1993 Single-electron capacitance spectroscopy of a few electron box *Phys. B: Condens. Matter* **189** 117–24

[17] Albrecht T R, Grütter P, Horne D and Rugar D 1991 Frequency modulation detection using high-*Q* cantilevers for enhanced force microscope sensitivity *J. Appl. Phys.* **69** 668–73

[18] van der Wiel W G, Franceschi S D, Elzerman J M, Fujisawa T, Tarucha S and Kouwenhoven L P 2002 Electron transport through double quantum dots *Rev. Mod. Phys.* **75** 1–22

[19] Hanson R, Kouwenhoven L P, Petta J R, Tarucha S and Vandersypen L M K 2007 Spins in few-electron quantum dots *Rev. Mod. Phys.* **79** 1217–65

[20] Woodside M T and McEuen P L 2002 Scanned probe imaging of single-electron charge states in nanotube quantum dots *Science* **296** 1098–101

[21] Zhu J, Brink M and McEuen P L 2005 Frequency shift imaging of quantum dots with single-electron resolution *Appl. Phys. Lett.* **87** 242102

[22] Zhu J, Brink M and McEuen P L 2008 Single-electron force readout of nanoparticle electrometers attached to carbon nanotubes *Nano Lett.* **8** 2399–404

[23] Swart I, Liljeroth P and Vanmaekelbergh D 2016 Scanning probe microscopy and spectroscopy of colloidal semiconductor nanocrystals and assembled structures *Chem. Rev.* **116** 11181-219

[24] Stomp R, Miyahara Y, Schaer S, Sun Q, Guo H, Grutter P, Studenikin S, Poole P and Sachrajda A 2005 Detection of single-electron charging in an individual InAs quantum dot by noncontact atomic-force microscopy *Phys. Rev. Lett.* **94** 056802

[25] Cockins L, Miyahara Y, Bennett S D, Clerk A A, Studenikin S, Poole P, Sachrajda A and Grutter P 2010 Energy levels of few-electron quantum dots imaged and characterized by

atomic force microscopy *Proc. Natl Acad. Sci.* **107** 9496–501
[26] Brink M 2007 Imaging single-electron charging in nanostructures by low-temperature scanning force microscopy *PhD Thesis* Cornell University
[27] Tekiel A, Miyahara Y, Topple J M and Grutter P 2013 Room-temperature single-electron charging detected by electrostatic force microscopy *ACS Nano* **7** 4683–90
[28] Tekiel A A 2013 Ultra-high vacuum fabrication of nanoscale systems for studying single-electron charging by room-temperature atomic force microscopy *PhD Thesis* McGill University
[29] Roseman M and Grutter P 2000 Cryogenic magnetic force microscope *Rev. Sci. Inst.* **71** 3782
[30] Rugar D, Mamin H J and Guethner P 1989 Improved fiber-optic interferometer for atomic force microscopy *Appl. Phys. Lett.* **55** 2588
[31] Albrecht T R, Grutter P, Rugar D and Smith D P E 1992 Low-temperature force microscope with all-fiber interferometer *Ultramicroscopy* **42-44** 1638–46 (Part B)
[32] Labuda A, Miyahara Y, Cockins L and Grütter P 2011 Decoupling conservative and dissipative forces in frequency modulation atomic force microscopy *Phys. Rev.* B **84** 125433
[33] Poole P L, McCaffrey J, Williams R L, Lefebvre J and Chitrani D 2001 Chemical beam epitaxy growth of self-assembled InAs/InP quantum dots *J. Vac Sci. Technol.* **B19** 1467
[34] Drexler H, Leonard D, Hansen W, Kotthaus J P and Petroff P M 1994 Spectroscopy of quantum levels in charge-tunable InGaAs quantum dots *Phys. Rev. Lett.* **73** 2252–5
[35] Miller B T, Hansen W, Manus S, Luyken R J, Lorke A, Kotthaus J P, Huant S, Medeiros-Ribeiro G and Petroff P M 1997 Few-electron ground states of charge-tunable self-assembled quantum dots *Phys. Rev.* B **56** 6764–9
[36] Tarucha S, Austing D G, Honda T, Van Der Hage R J and Kouwenhoven L P 1996 Shell filling and spin effects in a few electron quantum dot *Phys. Rev. Lett.* **77** 3613
[37] Roy-Gobeil A, Miyahara Y and Grutter P 2015 Revealing energy level structure of individual quantum dots by tunneling rate measured by single-electron sensitive electrostatic force spectroscopy *Nano Lett.* **15** 2324–8
[38] Beenakker C W J 1991 Theory of coulomb-blockade oscillations in the conductance of a quantum dot *Phys. Rev.* B **44** 1646–56
[39] Tews M 2004 Electronic structure and transport properties of quantum dots *Ann. Phys., Lpz.* **13** 249–304
[40] Deshpande M, Sleight J, Reed M and Wheeler R 2000 Sequential tunneling and spin degeneracy of zero-dimensional states *Phys. Rev.* B **62** 8240–8
[41] Bonet E, Deshmukh M M and Ralph D C 2002 Solving rate equations for electron tunneling via discrete quantum states *Phys. Rev.* B **65** 045317
[42] Bennett S D, Cockins L, Miyahara Y, Grütter P and Clerk A A 2010 Strong electromechanical coupling of an atomic force microscope cantilever to a quantum dot *Phys. Rev. Lett.* **104** 017203
[43] Hölscher H, Gotsmann B, Allers W, Schwarz U, Fuchs H and Wiesendanger R 2001 Measurement of conservative and dissipative tip–sample interaction forces with a dynamic force microscope using the frequency modulation technique *Phys. Rev.* B **64** 075402
[44] Kantorovich L N and Trevethan T 2004 General theory of microscopic dynamical response in surface probe microscopy: from imaging to dissipation *Phys. Rev. Lett.* **93** 236102
[45] Rodrigues D A, Imbers J, Harvey T J and Armour A D 2007 Dynamical instabilities of a resonator driven by a superconducting single-electron transistor *New J. Phys.* **9** 84
[46] Cockins L, Miyahara Y, Bennett S D, Clerk A and Grutter P 2012 Excited-state spectroscopy on an individual quantum dot using atomic force microscopy *Nano Lett.* **12** 709–13
[47] Escott C C, Zwanenburg F A and Morello A 2010 Resonant tunnelling features in quantum dots *Nanotechnology* **21** 274018
[48] Natelson D, Yu L H, Ciszek J W, Keane Z K and Tour J M 2006 Single-molecule transistors: electron transfer in the solid state *Chem. Phys.* **324** 267–75
[49] Leturcq R, Stampfer C, Inderbitzin K, Durrer L, Hierold C, Mariani E, Schultz M G, von Oppen F and Ensslin K 2009 Franck–Condon blockade in suspended carbon nanotube quantum dots *Nat. Phys.* **5** 327–31
[50] Jung M, Hirakawa K, Kawaguchi Y, Komiyama S, Ishida S and Arakawa Y 2005 Lateral electron transport through single self-assembled InAs quantum dots *Appl. Phys. Lett.* **86** 33106
[51] Pioda A, Kičin S, Ihn T, Sigrist M, Fuhrer A, Ensslin K, Weichselbaum A, Ulloa S E, Reinwald M and Wegscheider W 2004 Spatially resolved manipulation of single electrons in quantum dots using a scanned probe *Phys. Rev. Lett.* **93** 216801
[52] Bleszynski A C, Zwanenburg F A, Westervelt R M, Roest A L, Bakkers E P A M and Kouwenhoven L P 2007 Scanned probe imaging of quantum dots inside InAs nanowires *Nano Lett.* **7** 2559–62
[53] Boyd E E, Storm K, Samuelson L and Westervelt R M 2011 Scanning gate imaging of quantum dots in 1D ultra-thin InAs/InP nanowires *Nanotechnology* **22** 185201
[54] Zhou X, Hedberg J, Miyahara Y, Grutter P and Ishibashi K 2014 Scanning gate imaging of two coupled quantum dots in single-walled carbon nanotubes *Nanotechnology* **25** 495703
[55] Gardner J, Bennett S D and Clerk A A 2011 Mechanically probing coherent tunneling in a double quantum dot *Phys. Rev.* B **84** 205316
[56] Dalacu D *et al* 2009 Directed self-assembly of single quantum dots for telecommunication wavelength optical devices *Laser Photon. Rev.* **4** 283–99
[57] Maltezopoulos T, Bolz A, Meyer C, Heyn C, Hansen W, Morgenstern M and Wiesendanger R 2003 Wave-function mapping of InAs quantum dots by scanning tunneling spectroscopy *Phys. Rev. Lett.* **91** 196804
[58] Kim J Y, Voznyy O, Zhitomirsky D and Sargent E H 2013 25th Anniversary article: colloidal quantum dot materials and devices: a quarter-century of advances *Adv. Mater.* **25** 4986–5010
[59] Kuemmeth F, Bolotin K I, Shi S-F and Ralph D C 2008 measurement of discrete energy-level spectra in individual chemically synthesized gold nanoparticles *Nano Lett.* **8** 4506–12
[60] Nishino T, Negishi R, Kawao M, Nagata T, Ozawa H and Ishibashi K 2010 The fabrication and single electron transport of Au nano-particles placed between Nb nanogap electrodes *Nanotechnology* **21** 225301
[61] Guttman A, Mahalu D, Sperling J, Cohen-Hoshen E and Bar-Joseph I 2011 Self-assembly of metallic double-dot single-electron device *Appl. Phys. Lett.* **99** 063113
[62] Akkerman H B, Naber R C G, Jongbloed B, van Hal P, Blom P W M, de Leeuw D M and de Boer B 2007 Electron tunneling through alkanedithiol self-assembled monolayers in large-area molecular junctions *Proc. Natl Acad. Sci.* **104** 11161–6
[63] Song H, Kim Y, Jeong H, Reed M A and Lee T 2010 Coherent tunneling transport in molecular junctions *J. Phys. Chem.* C **114** 20431–5
[64] von Delft J and Ralph D C 2001 Spectroscopy of discrete energy levels in ultrasmall metallic grains *Phys. Rep.* **345** 61–173

[65] Müller T, Güttinger J, Bischoff D, Hellmuller S, Ensslin K and Ihn T 2012 Fast detection of single-charge tunneling to a graphene quantum dot in a multi-level regime *Appl. Phys. Lett.* **101** 012104
[66] Henry C R 2015 2D-Arrays of nanoparticles as model catalysts *Catal. Lett.* **145** 731–49
[67] Giordano L and Pacchioni G 2011 Oxide films at the nanoscale: new structures, new functions, and new materials *Acc. Chem. Res.* **44** 1244–52
[68] Tekiel A, Topple J, Miyahara Y and Grütter P H 2012 Layer-by-layer growth of sodium chloride overlayers on an Fe(001)-p $(1 \times 1)O$ surface *Nanotechnology* **23** 505602
[69] Park H, Park J, Lim A K L, Anderson E H, Alivisatos A P and McEuen P L 2000 Nanomechanical oscillations in a single-C60 transistor *Nature* **407** 57–60
[70] Park J *et al* 2002 Coulomb blockade and the Kondo effect in single-atom transistors *Nature* **417** 722–5
[71] Kubatkin S, Danilov A, Hjort M, Cornil J, Brédas J-L, Stuhr-Hansen N, Hedegård P and Bjørnholm T 2003 Single-electron transistor of a single organic molecule with access to several redox states *Nature* **425** 698–701
[72] Yu L H and Natelson D 2004 Transport in single-molecule transistors: Kondo physics and negative differential resistance *Nanotechnology* **15** S517–24
[73] Koenraad P M and Flatté M E 2011 Single dopants in semiconductors *Nat. Mater.* **10** 91–100
[74] Sellier H, Lansbergen G, Caro J, Rogge S, Collaert N, Ferain I, Jurczak M and Biesemans S 2006 Transport spectroscopy of a single dopant in a gated silicon nanowire *Phys. Rev. Lett.* **97** 206805
[75] Fuechsle M, Miwa J A, Mahapatra S, Ryu H, Lee S, Warschkow O, Hollenberg L C L, Klimeck G and Simmons M Y 2012 A single-atom transistor *Nat. Nanotechnol.* **7** 242–6
[76] Teichmann K, Wenderoth M, Loth S, Ulbrich R, Garleff J, Wijnheijmer A and Koenraad P 2008 Controlled charge switching on a single donor with a scanning tunneling microscope *Phys. Rev. Lett.* **101** 076103
[77] Ashoori R C, Stormer H L, Weiner J S, Pfeiffer L N, Pearton S J, Baldwin K W and West K W 1992 Single-electron capacitance spectroscopy of discrete quantum levels *Phys. Rev. Lett.* **68** 3088–91
[78] Ashoori R C, Stormer H L, Weiner J S, Pfeiffer L N, Baldwin K W and West K W 1993 N -electron ground state energies of a quantum dot in magnetic field *Phys. Rev. Lett.* **71** 613–6
[79] Villis B J, Orlov A O, Jehl X, Snider G L, Fay P and Sanquer M 2011 Defect detection in nano-scale transistors based on radio-frequency reflectometry *Appl. Phys. Lett.* **99** 152106
[80] Chorley S J, Wabnig J, Penfold-Fitch Z V, Petersson K D, Frake J, Smith C G and Buitelaar M R 2012 Measuring the complex admittance of a carbon nanotube double quantum dot *Phys. Rev. Lett.* **108** 036802
[81] Frey T, Leek P, Beck M, Blais A, Ihn T, Ensslin K and Wallraff A 2012 Dipole coupling of a double quantum dot to a microwave resonator *Phys. Rev. Lett.* **108** 046807
[82] Hile S J, House M G, Peretz E, Verduijn J, Widmann D, Kobayashi T, Rogge S and Simmons M Y 2015 Radio frequency reflectometry and charge sensing of a precision placed donor in silicon *Appl. Phys. Lett.* **107** 093504
[83] Verduijn J, Vinet M and Rogge S 2014 Radio-frequency dispersive detection of donor atoms in a field-effect transistor *Appl. Phys. Lett.* **104** 102107
[84] Gonzalez-Zalba M F, Barraud S, Ferguson A J and Betz A C 2015 Probing the limits of gate-based charge sensing *Nat. Commun.* **6** 6084
[85] Gonzalez-Zalba M F, Shevchenko S N, Barraud S, Johansson J R, Ferguson A J, Nori F and Betz A C 2016 Gate-sensing coherent charge oscillations in a silicon field-effect transistor *Nano Lett.* **16** 1614–9
[86] Frake J C, Kano S, Ciccarelli C, Griffiths J, Sakamoto M, Teranishi T, Majima Y, Smith C G and Buitelaar M R 2015 Radio-frequency capacitance spectroscopy of metallic nanoparticles *Sci. Rep.* **5** 10858